

CHAPTER 3

Overview of numerical simulations

3.1. Flow around unsteady wings

The unsteady experiments of Mai & Hebler (2011); Hebler *et al.* (2013) and Lokatt (2017) have shown that aerodynamic non-linearities are related to the movement of transition over the suction side of the airfoil. Thus unsteady boundary layer dynamics play an important role in aerodynamic response of NLF airfoils. The present work aims to investigate the unsteady boundary layers with a particular focus on unsteady transition to shed light on the phenomenon of non-linear unsteady aerodynamic response. The airfoil used in the investigation is the ED36F128 (with a 13.8° flap deflection), designed at the Aeronautical and Vehicle Engineering department at KTH. It is a natural laminar flow airfoil, which has been used in several steady and unsteady experiments (Lokatt & Eller 2017; Lokatt 2017). The unsteady experiments using the airfoil have shown the non-linearities that appear to be typical of laminar airfoils (Lokatt 2017). The results of the steady and unsteady experiments using this airfoil have been made available to us by Dr. Eller and Dr. Lokatt. Non-linearities in the unsteady aerodynamic forces are observed for only a certain range of angle of attack α . Therefore a careful assessment of the data was needed in order to select the right parameter range where the relevant flow physics could be observed in the numerical simulations. The primary measurement in the experimental campaign has been through pressure taps located around airfoil for the calculation of unsteady aerodynamic forces. Thus a measurement of the unsteady boundary layer characteristics is not available through the experimental data. Calculations using an integral boundary layer code XFOIL (Drela 1989) are used to complement the experimental data and better evaluate the state of the boundary layer in the static measurements.

Figure 3.1a shows the calculated transition locations for two different Reynolds numbers ($Re_c = 100,000$ and $Re_c = 750,000$) using XFOIL and figure 3.1b shows the experimentally measured normal force coefficient as well as calculations from XFOIL for $Re_c = 750,000$. For the higher Reynolds number case, transition location varies sharply with angle of attack within the range $3.4 < \alpha < 6.5$. Aerodynamic non-linearities can also be observed approximately within the same angle of attack range (figure 3.1b). On the other hand, for the lower Reynolds number case, no experimental data is available. Therefore solely

XFOIL calculations are used and the parameter range is selected where the transition location varies rapidly with angle of attack. This range is found to be for $6.7^\circ < \alpha < 8.0^\circ$. Numerical simulations are performed with stationary airfoils

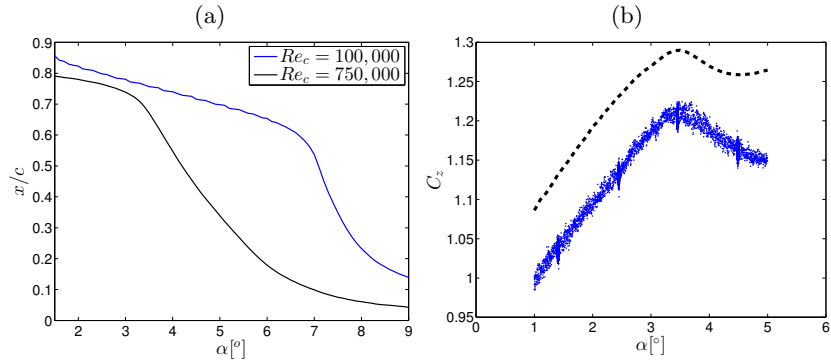


Figure 3.1: (a) Transition location calculated using XFOIL for two different Reynolds numbers. (b) Normal force coefficient measured in experiments (dots) and from XFOIL calculations (dashed line) for $Re_c = 750,000$.

to ensure the expected static boundary layer characteristics are captured by the numerical simulations. Figure 3.2 shows the instantaneous vortical structures in the flow for $Re_c = 750,000$ for an angle of attack $\alpha = 2.4^\circ$ and $\alpha = 4.4^\circ$ which shows the change in boundary layer characteristics in the static cases. Similarly figure 3.3 shows the static boundary layer characteristics for $Re_c = 100,000$ at $\alpha = 6.7^\circ$ and $\alpha = 8.0^\circ$.

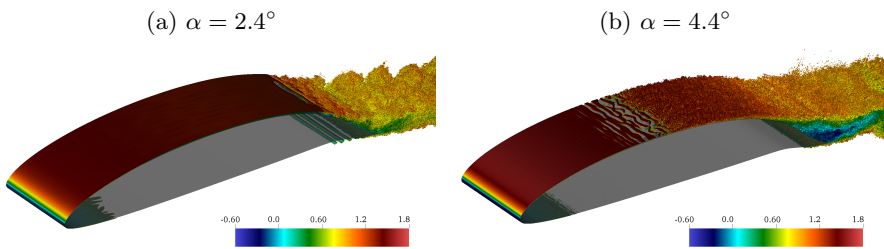


Figure 3.2: Instantaneous vortical structures identified by the λ_2 criterion for the two stationary angle of attack simulations at $Re_c = 750,000$.

For both the Reynolds number cases, significant temporal variation of transition location is also found for the unsteady cases. Figure 3.4 shows the

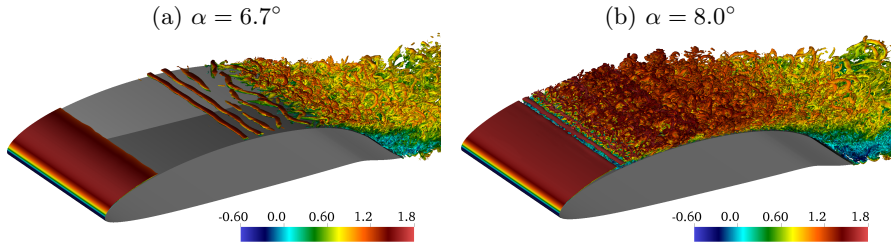


Figure 3.3: Isocontours of instantaneous λ_2 structures observed for two different (stationary) angles of attack at $Re_c = 100,000$.

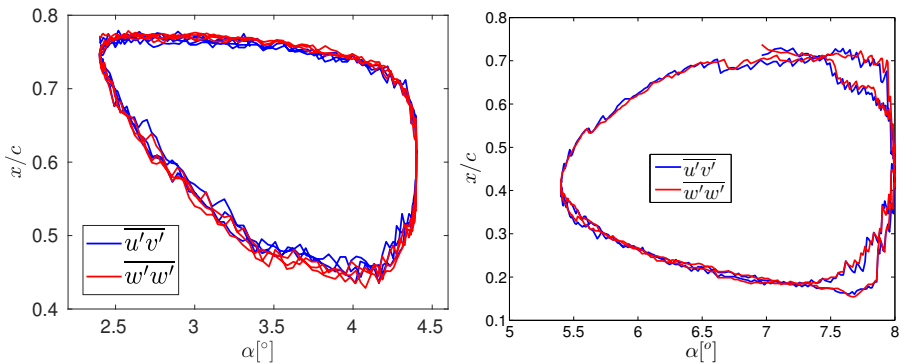


Figure 3.4: Phase portraits of transition location for (left) $Re_c = 750,000$ and (right) $Re_c = 100,000$.

variation of transition with respect to α . The transition locations were calculated using thresholds on the instantaneous spanwise-averaged Reynolds stress $\overline{u'v'}$ and spanwise fluctuation intensity $\overline{w'w'}$. For the lower Reynolds number case the boundary also develops a leading-edge laminar separation bubble during the pitch cycle which significantly influences the boundary layer dynamics.

3.2. Flow around a stationary wing section

The final paper in the thesis deals with the study of the boundary layer over a wing section at a chord-based Reynolds number of $Re_c = 1,000,000$. The airfoil used for the study is the asymmetric NACA 4412. A DNS database of for the flow around the same airfoil at $Re_c = 400,000$ is available and comparisons are made between the two cases to assess the effects of changing Reynolds number on the developing boundary layer. The numerical setup is done in a manner very similar to the computational study by Hosseini *et al.* (2016). Figure 3.5 shows a section of the numerical grid and the instantaneous vortical structures in the flow field. Figure 3.6 shows a comparison of the different measures of

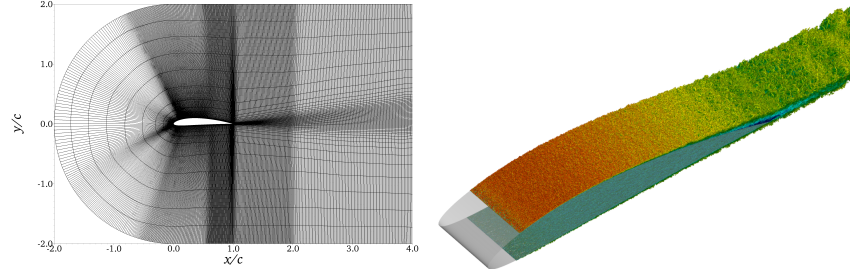


Figure 3.5: (Left) Two-dimensional slice of the computational domain showing the spectral-element distribution, but not the individual GLL points. (Right) Instantaneous flow field showing coherent structures identified with the λ_2 method (Jeong & Hussain 1995), and colored with horizontal velocity. In this figure, dark blue represents a horizontal velocity of -0.1 and dark red a value of 2 .

the boundary layer over the chord-wise distance for the two different Reynolds numbers. While both wall-shear stress (indicated by Re_τ) and boundary layer thickness (measured with momentum thickness Reynolds number Re_θ) change between the two cases, the Clauser parameter stays nearly the same throughout the chord. This allows comparisons across different Reynolds numbers without ambiguity since the pressure gradient histories remain the same with changing Reynolds numbers.

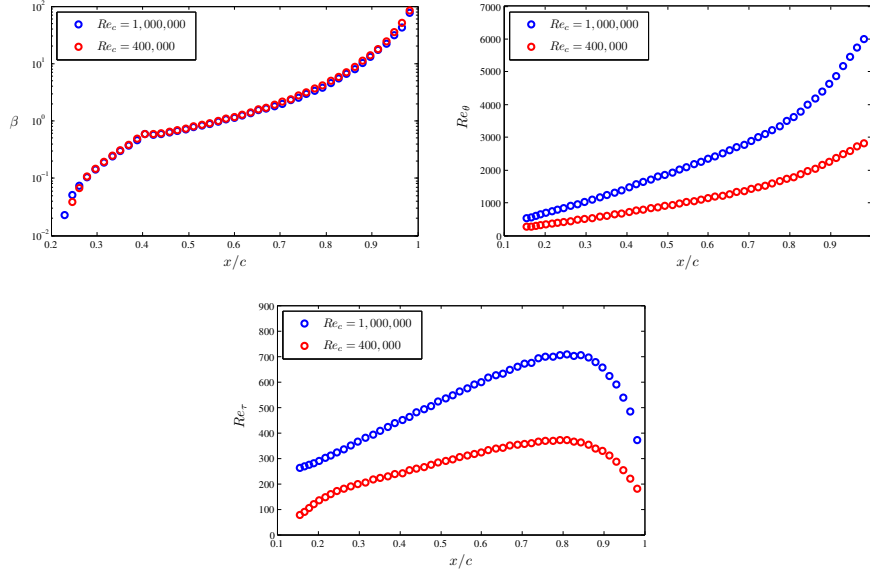


Figure 3.6: Streamwise evolution of (top left) the Clauser pressure-gradient parameter β , (top right) the Reynolds number based on momentum thickness Re_θ and (bottom) the friction Reynolds number Re_τ , for the two wing cases under study.